Available online at www.sciencedirect.com
ScienceDirect
Journal of Computational Physics 227 (2008) 5816–5835
JOURNAL OF COMPUTATIONAL PHYSICS
www.elsevier.com/locate/jcp

Viscous regularization and r-adaptive remeshing for finite element analysis of lipid membrane mechanics

Lin Ma, William S. Klug *

Department of Mechanical and Aerospace Engineering, University of California, Los Angeles, Los Angeles, CA 90095, United States

Received 5 September 2007; received in revised form 19 December 2007; accepted 12 February 2008
Available online 29 February 2008

Abstract

As two-dimensional fluid shells, lipid bilayer membranes resist bending and stretching but are unable to sustain shear stresses. This property gives membranes the ability to adopt dramatic shape changes. In this paper, a finite element model is developed to study static equilibrium mechanics of membranes. In particular, a viscous regularization method is proposed to stabilize tangential mesh deformations and improve the convergence rate of nonlinear solvers. The augmented Lagrangian method is used to enforce global constraints on area and volume during membrane deformations. As a validation of the method, equilibrium shapes for a shape-phase diagram of lipid bilayer vesicle are calculated. These numerical techniques are also shown to be useful for simulations of three-dimensional large deformation problems: the formation of tethers (long tube-like extensions); and Ginzburg–Landau phase separation of a two lipid-component vesicle. To deal with the large mesh distortions of the two-phase model, modification of viscous regularization is explored to achieve r-adaptive mesh optimization.

PACS: 87.16.Dg; 87.16.Ac; 02.70.Dh; 46.15.−x; 46.70.Hg

Keywords: Biomembranes; Lipid bilayer mechanics; Finite element; Artificial viscosity; r-Adaptive remeshing

1. Introduction

Lipid membranes are a critical part of life because they serve as a barrier to separate the contents of the cell from the external world. Lipid molecules are composed of a hydrophilic headgroup and two hydrophobic hydrocarbon chains [1], and will form a bilayer structure spontaneously by the hydrophobic effect when introduced into water in sufficient concentration. Though the cell membrane has more complex structure, being littered with all kinds of proteins that serve as selective receptors, channels and pumps, in this paper we will focus on closed spherical pure lipid bilayer membranes, i.e., vesicles.

DOI of original article: 10.1016/j.jcp.2006.05.023.
* Corresponding author.
E-mail addresses: linm@seas.ucla.edu (L. Ma), klug@ucla.edu (W.S. Klug).

0021-9991/$ - see front matter © 2008 Elsevier Inc. All rights reserved.
doi:10.1016/j.jcp.2008.02.019

Common experience reveals that it is much easier to bend a thin plate than to stretch it (a good example is a sheet of paper). This is also true for lipid bilayer membranes, except that there is no shear force because of the fluid property of membranes. The mechanical energy of a lipid bilayer has three major contributors: bending (curvature) of each monolayer; area or in-plane expansion and contraction of each monolayer; and osmotic pressure. Because the last two energy scales are much larger than the first one (by several orders of magnitude) [2], they effectively place constraints on the total surface area and enclosed volume of the bilayer membrane on experimental time scales (up to at least 1 h). Thus, the mechanically interesting energy arises from bending of the membrane.

Canham [3], Helfrich [4] and Evans [5] pioneered the development of the lowest-order bending energy theory, often referred to as the spontaneous curvature model, in which energy is a quadratic function of the principle curvatures and the intrinsic or *spontaneous* curvature of the surface. Incremental improvements to this model include the bilayer couple model [6,7], which imposes the hard constraint on the area difference of the two monolayers, and the area-difference-elasticity (ADE) model [8–10], which adds a non-local curvature energy term representing an elastic penalty on the area difference.

The equations of equilibrium for the spontaneous curvature model, first calculated by Jenkins [11,12], are difficult to solve being highly nonlinear fourth-order PDEs. The most common approach to modeling membrane mechanics numerically has been to discretize a vesicle surface by a triangle mesh, and approximate the curvature along mesh edges with finite-difference (FD) operators. Starting from some suitable initial shape, the FD approximation of curvature energy can be summed on the triangulation, and an adjacent local minimum then can be found by downhill minimization (often via a conjugate gradient algorithm) [13–16]. Another mesh-based approach, the finite element method (FEM), was also recently applied to the study of membrane mechanics by Feng and Klug [17], using C^1-conforming triangular subdivision surfaces elements to approximate the membrane curvature energy.

One feature shared in common among these mesh-based methods is the need for stabilization of mesh vertex motions tangential to the discretized surface. This issue arises as a fundamental consequence of the use of a mesh for explicit coordinate parameterization of the geometry of a fluid membrane having no physically meaningful reference configuration. As pointed out previously (e.g. [18,19]), the dependence of the curvature energy functional on the surface position map is invariant upon changes in parameterization. Physically, this implies that in-plane dilatational and shear modes of mesh deformation carry no energy cost, and therefore, no stiffness. The addition of an artificial in-plane stiffness, for example by placing Hookean springs along the edges of a triangular mesh [18] does indeed stabilize these motions, but in doing so also changes the physics, yielding a model for a polymerized (rather than fluid) membrane. In order to allow for fluid-like diffusion of membrane vertices, a number of researchers have used a *dynamic triangulation* approach, wherein the edge connecting a pair of adjacent triangles along one of the diagonals between the four associated vertices is swapped for the other diagonal. Within a Monte Carlo simulation framework this method yields mean-square vertex displacements that are consistent with microscopic diffusion [20], and this approach has been shown to produce an effective viscosity that increases as the edge swapping rate decreases [21]. However, it is unclear whether the dynamic triangulation approach can enable unphysical in-plane forces to fully relax to zero in a *zero-temperature* energy minimization context as is adopted here.

Alternatively, as shown in the finite element (FE) context [17], tangential vertex motions may be suppressed partially by enforcing the incompressibility of the membrane as a local (rather than global) area constraint. This approach also allows for diffusion of vertices; however, local enforcement of incompressibility can lead to severe distortion of elements in the mesh, and therefore hinders the simulation of large vesicle deformations. Furthermore, local incompressibility does not completely suppress spurious modes, and though these degeneracies do not prevent simulation of unforced vesicle equilibrium, they can lead to catastrophic numerical instabilities when externally applied forces are introduced.

Notably, these issues may be avoided entirely through the development of meshless numerical methods for membrane mechanics. Examples include, Ritz methods with global basis functions (e.g. spherical harmonics) [3,22,23], phase field methods [24,25] and moving-least squares approximation [26]. Yet, these approaches are not without their own limitations (e.g. aliasing, difficulty with application of external forces).

In this paper we propose a viscous regularization technique to stabilize tangential motions of nodes in a FE membrane model while enforcing incompressibility as a global constraint. We demonstrate the computational

efficiency and effectiveness of this approach by comparing simulation times with and without regularization for shape transitions previously computed in [17]. Secondly, we examine the efficiency gained by enforcing the *global* constraints on membrane area and volume with an augmented Lagrangian approach instead of the previous penalty approach. Lastly, we apply the regularization and constraint methods to the simulation of two membrane shape change problems involving large deformations and the application of external forces. The first of these problems is the simulation of the tether instability in a vesicle under tension between two opposing point forces; the second is the simulation of separation and domain formation in a two lipid-phase vesicle. In the latter we demonstrate how the viscous regularization technique can be slightly modified to formulate an r-adaptive remeshing method, wherein nodes "flow" on the surface of the vesicle in such a way as to avoid element distortion.

The outline of this paper is as follows: Section 2 briefly introduces the FEM formulation for bilayer membrane mechanics along with artificial viscosity mesh stabilization and augmented Lagrangian constraint enforcement. Section 3 shows two applications: tether formation and lipid phase separation, based on the methods described in Section 2. Section 4 concludes with discussions of results and future applications.

2. Methods

2.1. Lipid bilayer mechanics and finite element approximation

We begin with a brief review of the mechanics of bilayer membranes and FEM approximation we use. For further details, the reader is referred to [17].

2.1.1. Membrane kinematics

The bilayer membrane is described as a two-dimensional surface $\mathcal{M}$ embedded in three-dimensional space (Fig. 1), parameterized by curvilinear coordinates $\{s^1, s^2\}$, such that its position is given by the map $\boldsymbol{x} : \mathbb{R}^2 \to \mathbb{R}^3$. With standard definitions from differential geometry [27,28], we can span the surface tangent plane with both (covariant) basis vectors $\boldsymbol{a}_\alpha = \frac{\partial \boldsymbol{x}}{\partial s^\alpha} \equiv \boldsymbol{x}_{,\alpha}$ and dual (contravariant) basis vectors $\boldsymbol{a}^\alpha$ defined such that $\boldsymbol{a}^\alpha \cdot \boldsymbol{a}_\beta = \delta^\alpha_\beta$. The covariant and contravariant surface metric tensors are then

$$a_{\alpha\beta} = \boldsymbol{a}_\alpha \cdot \boldsymbol{a}_\beta, \quad \text{and} \quad a^{\alpha\beta} = \boldsymbol{a}^\alpha \cdot \boldsymbol{a}^\beta, \tag{1}$$

and the determinant of the covariant metric tensor will be denoted

$$a = \det a_{\alpha\beta}. \tag{2}$$

The normal to the surface is

$$\boldsymbol{d} \equiv \boldsymbol{a}_3 = \frac{\boldsymbol{a}_1 \times \boldsymbol{a}_2}{|\boldsymbol{a}_1 \times \boldsymbol{a}_2|} = \frac{\boldsymbol{a}_1 \times \boldsymbol{a}_2}{\sqrt{a}}. \tag{3}$$

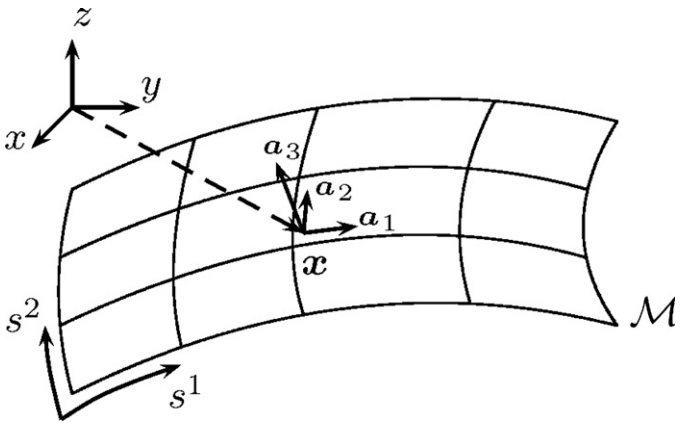

Fig. 1. Geometry of a surface.

The curvature tensor $\mathbf{B}$ is defined by its covariant components

$$b_{\alpha\beta} = -\boldsymbol{d}_{,\alpha} \cdot \boldsymbol{a}_\beta = \boldsymbol{d} \cdot \boldsymbol{x}_{,\alpha\beta} = \boldsymbol{d} \cdot \boldsymbol{a}_{\alpha,\beta}. \tag{4}$$

The mean curvature is one half of the trace of the curvature tensor

$$H = \frac{1}{2} b^\alpha_\alpha = \frac{1}{2} a^{\alpha\beta} b_{\alpha\beta} = -\frac{1}{2} a^{\alpha\beta} (\boldsymbol{d}_{,\alpha} \cdot \boldsymbol{a}_\beta) = -\frac{1}{2} \boldsymbol{a}^\alpha \cdot \boldsymbol{d}_{,\alpha} \tag{5}$$

(where $a^{\alpha\beta} a_{\alpha\beta} = \delta^\alpha_\beta$), and the Gaussian curvature is the determinant of the curvature tensor

$$K = \det \mathbf{B} = \det b_{\alpha\beta}. \tag{6}$$

2.1.2. Lipid bilayer mechanics

We describe the energetics of the membrane by the Helfrich model [4], which assumes a strain energy of the form

$$E[\boldsymbol{x}] = \int_{\mathcal{M}} \frac{1}{2} \mathcal{K}_C (2H - C_0)^2 \sqrt{a}\, \mathrm{d}^2 s + \int_{\mathcal{M}} \mathcal{K}_G K \sqrt{a}\, \mathrm{d}^2 s, \tag{7}$$

where $\mathcal{K}_C$ is the bending modulus and $\mathcal{K}_G$ is the Gaussian curvature modulus. By the Gauss–Bonnet theorem [27], the integral of Gaussian curvature is a topological constant $\int_{\mathcal{M}} K \sqrt{a}\, \mathrm{d}^2 s = 4\pi(1 - g)$, with g being the genus, i.e. the number of handles, and thus can be neglected.

The weak form of equilibrium for the membrane can be obtained in general by the principle of virtual work, and for the case of conservative loads by minimization of total potential energy. The later dictates that the total potential energy by stationary with respect to any arbitrary admissible surface variation $\delta\boldsymbol{x}$

$$\delta \Pi \equiv \delta E - \delta W^{\mathrm{ext}} = 0. \tag{8}$$

Here δE is the first variation of the membrane bending energy, and $\delta W^{\mathrm{ext}} = \int_{\mathcal{M}} \boldsymbol{f}^{\mathrm{ext}} \cdot \delta\boldsymbol{x} \sqrt{a}$ is the virtual work done by conservative external forces $\boldsymbol{f}^{\mathrm{ext}}$. A straightforward calculation [17] gives the first variation of the total energy as

$$\delta \Pi = \int_{\mathcal{M}} [\boldsymbol{n}^\alpha \cdot \delta \boldsymbol{a}_\alpha + \boldsymbol{m}^\alpha \cdot \delta \boldsymbol{d}_{,\alpha} - \boldsymbol{f}^{\mathrm{ext}} \cdot \delta \boldsymbol{x}] \sqrt{a}\, \mathrm{d}^2 s, \tag{9}$$

where we have defined stress resultants $\boldsymbol{n}^\alpha$ and moment resultants $\boldsymbol{m}^\alpha$ as

$$\boldsymbol{n}^\alpha = \mathcal{K}_C (2H - C_0) a^{\alpha\beta} \boldsymbol{d}_{,\beta} + \mathcal{K}_C \frac{1}{2} (2H - C_0)^2 \boldsymbol{a}^\alpha, \quad \boldsymbol{m}^\alpha = -\mathcal{K}_C (2H - C_0) \boldsymbol{a}^\alpha. \tag{10}$$

2.1.3. Enforcing constraints

Admissibility requirements on trial functions $\boldsymbol{x}$ and variations $\delta\boldsymbol{x}$ include the satisfaction of any active constraints, such as the aforementioned constraints on total surface area and enclosed volume. Here we will enforce these constraints with the augmented Lagrangian (AL) approach (see, e.g. [29]). The AL method may be thought of as a hybrid between penalty and Lagrange multiplier methods. The basic idea of AL is to solve iteratively for a Lagrange multiplier, computing multiplier updates from a penalty term.

To enforce constraints on both area and volume of a membrane, we establish a sequence of modified energy functionals, the nth of these taking the form $I^n = \Pi + I^{\mathrm{con}}$, where I^{con} is a constraint energy term

$$I^{\mathrm{con}} = \frac{\mu_V}{2} (V - \overline{V})^2 - p^n V + \frac{\mu_A}{2} (A - \overline{A})^2 + \alpha^n A.$$

Here $\overline{A}$ and $\overline{V}$ are the specified surface area and enclosed volume of the membrane, μ_A and μ_V are penalty parameters (large and positive), and α^n and p^n are tension and pressure multiplier estimates for the nth iteration. Minimization of the modified energy (holding multiplier estimates fixed) yields

$$\delta I^n = \delta \Pi - p^{n+1} \delta V + \alpha^{n+1} \delta A = 0,$$

where $p^{n+1} = p^n - \mu_V(V_n - \overline{V})$ and $\alpha^{n+1} = \alpha^n + \mu_A(A_n - \overline{A})$ are the updated multiplier estimates. Iteration of minimization followed by multiplier updates is continued until constraints are satisfied to within some preselected tolerance, TOL. In this way the modified energy converges to the pure Lagrange multiplier constrained functional, with the added benefit of avoiding the associated saddle-point problem, retaining a minimization structure which is convenient for nonlinear optimization algorithms.

Whereas pure penalty methods require very large penalty parameters for accurate constraint enforcement, the AL iterative updates can achieve accuracy with much smaller penalty terms. In practice this is an important advantage, since large penalty parameters μ_V and μ_A make numerical minimization difficult as the Hessian $\nabla^2 E$ (or stiffness matrix) becomes ill conditioned [29]. Here, we follow common practice of incrementally increasing the initially small penalty parameters by a factor, FAC, after each AL iteration to achieve faster convergence.

2.1.4. Finite element approximation

A FE approximation is introduced by replacing the field $\boldsymbol{x}$ with the approximated field $\boldsymbol{x}_h$ defined by

$$\boldsymbol{x}_h(s^1, s^2) = \sum_{a=1}^{N} \boldsymbol{x}_a N^a(s^1, s^2), \tag{11}$$

where the $N^a(s^1, s^2),\ a = 1, \ldots, N$ are *shape functions* of the FE mesh, and their coefficients, $\boldsymbol{x}_a$ are the positions of the nodal control vertices. Introducing this approximation into the modified energy functional upon minimization leads to a set of discrete approximate equilibrium equations

$$\boldsymbol{f}_a^{\text{int}} + \boldsymbol{f}_a^{\text{con}} - \boldsymbol{f}_a^{\text{ext}} = 0. \tag{12}$$

Here $\boldsymbol{f}_a^{\text{int}}$ are the *internal* nodal forces due to bending of the membrane,

$$\boldsymbol{f}_a^{\text{int}} = \int_{\mathcal{M}} \left[\boldsymbol{n}^\alpha \cdot \frac{\partial \boldsymbol{a}_\alpha}{\partial \boldsymbol{x}_a} + \boldsymbol{m}^\alpha \cdot \left(\frac{\partial \boldsymbol{d}}{\partial \boldsymbol{x}_a} \right)_{,\alpha} \right] \sqrt{a}\, \mathrm{d}^2 s, \tag{13}$$

$\boldsymbol{f}_a^{\text{con}}$ are the *constraint* nodal forces due to the pressure and tension that are conjugate to the constrained volume and area,

$$\boldsymbol{f}_a^{\text{con}} = -p^{n+1} \frac{\partial V}{\partial \boldsymbol{x}_a} + \alpha^{n+1} \frac{\partial A}{\partial \boldsymbol{x}_a}, \tag{14}$$

and $\boldsymbol{f}_a^{\text{ext}}$ are the *external* nodal forces, due to the application of distributed loads on the surface,

$$\boldsymbol{f}_a^{\text{ext}} = \int_{\mathcal{M}} \boldsymbol{f}^{\text{ext}} N^a \sqrt{a}\, \mathrm{d}^2 s. \tag{15}$$

Note that the integrands of the global expressions for internal and constraint forces are described in more explicit detail in [17]. Following that work, we again employ C^1-conforming subdivision surface shape functions [30,31] along with second-order (three-point) Gaussian quadrature for the computation of element integrals.

2.2. Viscous regularization of tangential mesh deformation

In the curvature model, the energy is determined by the mean curvature which is a parameterization-independent property of the surface shape, and thus is not sensitive to in-plane dilatational or shearing deformations of the surface FE mesh. Much like physical lipid molecules, FE nodes can flow freely on the deformed surface. As discussed in [17], this fact is manifested in the appearance of degenerate, zero-stiffness, zero-energy modes. Here we discuss the implementation of an artificial viscosity method designed to numerically eliminate these degenerate modes.

For solid shells having both reference and deformed configurations, in-plane deformations (dilatation and shearing) can thus be expressed locally in terms of first derivatives of the surface position maps of these two configurations. In curvature model,a well-defined reference configuration does not exist since the energy is only related to the deformed shape. The basic ingredients for stabilization of these tangential modes are

the introduction of a reference configuration and an energy term elastically penalizing in-plane deformation away from this reference state. However, to retain the physics of the original model, the addition of any in-plane elastic energy must result in a variational problem possessing the same minimizing solution as the original problem. In other words, the artificial in-plane energy must attain a value of zero when the entire model is in equilibrium. To design an algorithm that achieves these goals, we define a sequence of variational problems, minimizing a modified energy functional

$$I^n = \Pi[\boldsymbol{x}] + I^{\mathrm{con}}[\boldsymbol{x}] + I^{\mathrm{reg}}[\boldsymbol{x}; \boldsymbol{X}^n], \tag{16}$$

where the reference configuration $\boldsymbol{X}^n$ for the nth iteration is the deformed solution $\boldsymbol{x}^{n-1}$ of the previous iteration. The form of the regularization energy $I^{\mathrm{reg}}[\boldsymbol{x}; \boldsymbol{X}]$ can be chosen such that it vanishes when $\boldsymbol{x} = \boldsymbol{X}$, to ensure that solutions $\boldsymbol{x}^n$ converge to minimizers of the original unregularized problem with increasing n. This regularization method is outlined below in the following algorithm.

Algorithm 1. Viscous regularization via reference updates

Set $X^0 =$ initial shape
Set $n = 0$
repeat
  Minimize $I^n = \Pi[\boldsymbol{x}] + I^{\mathrm{con}}[\boldsymbol{x}] + I^{\mathrm{reg}}[\boldsymbol{x}; \boldsymbol{X}^n] \rightarrow$ solution, $\boldsymbol{x}^n$
  Update reference: set $\boldsymbol{X}^{n+1} = \boldsymbol{x}^n$
  $n \leftarrow n + 1$
until $I^{\mathrm{reg}}[\boldsymbol{x}^n; \boldsymbol{X}^n] <$ TOL

Qualitatively, assignment of the reference configuration for each iteration to be the current configuration of the previous iteration results in a type of algorithmic viscosity, producing forces that resist the motion of nodes away from their position at each previous iteration. The quantitative details of this viscosity depend on the particular form chosen for the in-plane regularization energy, I^{reg}. Here we give two example forms, the first derived from planar continuum elasticity theory and the second representing the mesh as a network of viscous dashpot elements.

2.2.1. Continuum elastic regularization energy

Here we treat the in-plane deformation response for each regularization iteration as that of a two-dimensional solid membrane. This local response can be modeled via a hyperelastic strain energy density, $w(\mathbf{F})$, which is a function of the surface deformation gradient

$$\mathbf{F} = \boldsymbol{a}_\alpha \otimes \boldsymbol{A}^\alpha, \tag{17}$$

where $\boldsymbol{A}^\alpha$ are the dual basis vectors on the reference surface, i.e., $\boldsymbol{A}^\alpha \cdot \boldsymbol{A}_\beta = \delta^\alpha_\beta$, where $\boldsymbol{A}_\alpha = \boldsymbol{X}^n_{,\alpha}$. Thus, the regularization energy becomes

$$I^{\mathrm{reg}}[\boldsymbol{x}; \boldsymbol{X}^n] = \int_{\mathcal{M}} w(\mathbf{F}) \sqrt{A}\, \mathrm{d}^2 s. \tag{18}$$

To preserve objectivity, the strain energy is a function of $\mathbf{F}$ through implicit dependence on the invariants of the surface-Right-Cauchy-Green deformation tensor $\mathbf{C} = \mathbf{F}^{\mathsf{T}} \cdot \mathbf{F} = a_{\alpha\beta} \boldsymbol{A}^\alpha \otimes \boldsymbol{A}^\beta$ [32]. As $\mathbf{C}$ is a rank-2 tensor, the two non-zero principal invariants are

$$I_1 = \mathrm{tr}(\mathbf{C}) = \bar{a}^{\alpha\beta} a_{\alpha\beta}, \tag{19a}$$

$$I_2 = \frac{1}{2}\{[\mathrm{tr}(\mathbf{C})]^2 - \mathrm{tr}(\mathbf{C}^2)\} = \frac{1}{2}\{(\bar{a}^{\alpha\beta} a_{\alpha\beta})^2 - \bar{a}^{\alpha\mu} \bar{a}^{\beta\nu} a_{\alpha\beta} a_{\mu\nu}\} \equiv J^2. \tag{19b}$$

The strain energy density is thus a function of these two invariants

$$w(\mathbf{F}) = w(I_1, I_2).$$

As a specific example, consider a strain energy function that decouples the dilatational, and shear responses, as used by Evans and Skalak [33] to model the red blood cell cytoskeleton

$$w = \underbrace{\frac{k}{2}(J-1)^2}_{\text{area change}} + \underbrace{\mu\left(\frac{\mathrm{tr}(\mathbf{C})}{2J} - 1\right)}_{\text{shear}}.$$

Here k and μ are stretching and shear moduli, respectively. It should be carefully noted that although we follow here the formalism of solid mechanics, the reference configuration $\boldsymbol{X}^n$ is not permanent as for a solid; rather the reference configuration is iteratively updated so that the resulting stresses may relax to zero.

2.2.2. Dashpot regularization energy

The viscous character of our proposed scheme is much more obvious when we compose the regularization energy of contributions from Hookean springs placed along all element edges, namely,

$$I^{\mathrm{reg}} = \sum_{\text{edge } ab} \frac{k}{2}(\ell_{ab} - L_{ab})^2, \tag{20}$$

where $\ell_{ab} = |\boldsymbol{x}_a - \boldsymbol{x}_b|$ and $L_{ab} = |\boldsymbol{X}_a^n - \boldsymbol{X}_b^n|$ are the lengths of the edge connecting mesh vertices a and b in the deformed and current configurations, respectively. Differentiating this energy, the corresponding force on a node a from the spring connecting it along an edge to node b can be obtained as

$$\boldsymbol{f}_{ab} = k(\ell_{ab} - L_{ab})\boldsymbol{n}_{ab},$$

where $\boldsymbol{n}_{ab}$ is the unit vector pointing from node a to node b. Recalling that the reference configuration for the nth iteration is the same as the deformed configuration of the $n-1$th iteration, the magnitude of this force can also be written as

$$f_{ab} = k(\ell_{ab}^n - \ell_{ab}^{n-1}).$$

This is easily identified as the backward-Euler time-discretization of the force–velocity relation for a viscous dashpot

$$f_{ab} = k\frac{\partial \ell_{ab}}{\partial t},$$

Thus, iterative reference updates of the form $\boldsymbol{X}^n = \boldsymbol{x}^{n-1}$ have the effect of converting a network of springs into a network of dashpots, clearly revealing the viscous character of the regularization scheme.

We have numerically implemented both the continuum elastic and dashpot regularization described here, and although both forms are effective in practice we have preferred the dashpot approach for its simplicity, efficiency and robustness. The remainder of the paper focuses on the use of this second approach, demonstrating its effectiveness in application.

3. Applications

3.1. Shape vs. reduced volume

Even in the absence of any externally applied loads, the two constraints on area and volume cause vesicles to transition among a variety of interesting equilibrium shapes. Here some of the calculations performed in [17] of the equilibrium shapes for different reduced volumes are repeated, as a first demonstration of the effectiveness of viscous regularization.

Reduced volume v is a geometrical quantity defined as

$$v = \frac{V}{(4\pi/3)R_0^3}, \tag{21}$$

where $R_0 = \sqrt{A/4\pi}$ is the radius of a sphere with the area A of the vesicle, called the equivalent sphere radius. Reduced volume is then written as

$$v = \frac{6\sqrt{\pi}V}{A^{3/2}}. \tag{22}$$

The reduced volume is the ratio of the current volume of the vesicle and the maximum volume that the current total area of vesicle can ensphere. For a spherical vesicle, the reduced volume $v = 1$; a vesicle of any other shape has $0 < v < 1$.

To compute the following results, the spontaneous curvature model is used with $C_0 = 0$. The modified energy is computed with loop subdivision shell elements and second-order (three-point) Gaussian quadrature, and minimized with the quasi-newton L-BFGS-B solver [34–36].

3.1.1. Viscous regularization

As a first assessment of the benefit of regularization, results are compared with the simulations done in [17], in which local area and global volume constraints were performed by penalty method instead of AL method. First, the same calculation of [17] is repeated; then the viscous regularization is added, with same kind of constraints (local area and global volume constraint) and penalty parameters ($\mu_A = 10^4 \mathcal{K}_C / R_0^4$ for local area constraint and $\mu_V = 5 \times 10^4 \mathcal{K}_C / R_0^6$ for global volume constraint).

The calculation starts from an initial ellipsoid shape which has a reduced volume $v = 0.914$ (Fig. 2). In the calculation, the area is fixed at its initial value and the volume is reduced in order to satisfy the constraint on v. For each simulation, violation of the volume constraint subjects the vesicle to a large pressure according to the penalty term in the functional. The energy is then relaxed by L-BFGS-B minimization and result in the equilibrium shapes. The iteration of reference updates in Algorithm 1 is continued until the regularization energy is sufficiently small, $I^{\text{reg}}/I < 10^{-5}$. In all the simulations, the same mesh, made up of 642 vertex nodes and 1280 elements, is used.

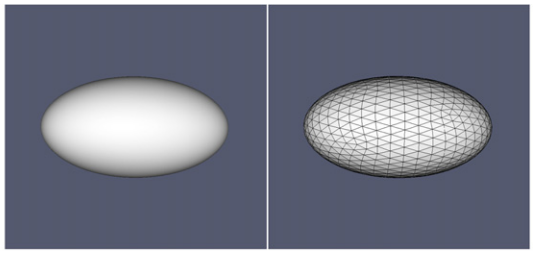

(a) Initial shape, $\nu = 0.914$ (not in equilibrium)

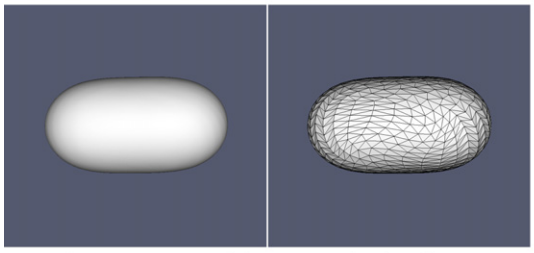

(b) $\nu = 0.9$ without regularization.

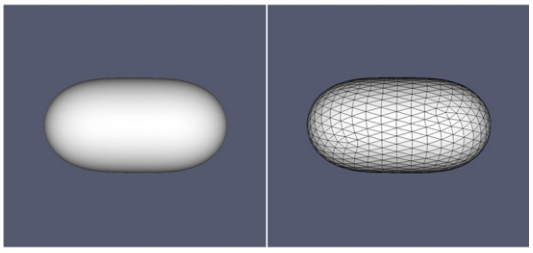

(c) $\nu = 0.9$ with regularization.

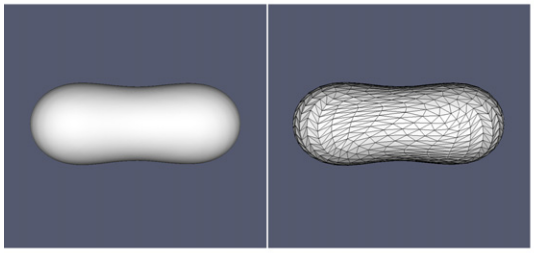

(d) $\nu = 0.8$ without regularization.

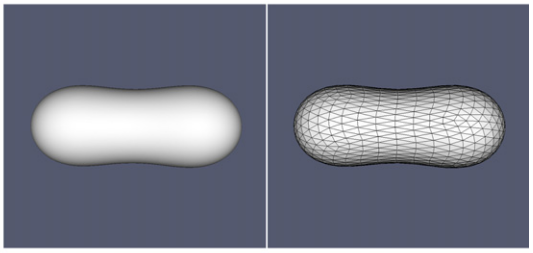

(e) $\nu = 0.9$ with regularization.

Fig. 2. Limit surfaces and control meshes of equilibrium shapes for $v = 0.9$ and 0.8.

The resulting equilibrium shapes for $v = 0.9$ and 0.8 are shown in Fig. 2. Starting from the initial shape, the equilibrium shape for $v = 0.9$ is computed by minimizing the energy; then from the resulting $v = 0.9$ shape, setting $v = 0.8$, the equilibrium shape for $v = 0.8$ is computed. The computational cost with and without the viscous regularization is listed in Table 1. As can be seen, the convergence rate is highly improved (almost two orders of magnitude faster) with the viscous regularization while the resulting shapes are equivalent. For different choices of spring constant k, the computational cost also varies. The computational cost has two contributions: one is the iteration number for each minimization; the other is the number of reference updates required to satisfy the convergence criterion $I^{\text{reg}}/I < 10^{-5}$. These both depend on k. For each minimization, the larger k is, the smaller the iteration number will be. While for the number of reference updates, it is opposite: the larger k is, the more reference updates needed. For example, to get the equilibrium shape $v = 0.9$ from the initial shape, $k = \mathcal{K}_C/R_0^2$ requires two reference updates, each of which costs ≈ 1000 iterations for minimization; while for $k = 100\mathcal{K}_C/R_0^2$, there are 20 reference updates each costing ≈ 250 minimization iterations. In this case $k = \mathcal{K}_C/R_0^2$ works the best, but the optimal k depends on the specific problem. In the later sections on tether formation, a much larger k ($k = 1000\mathcal{K}_C/R_0^2$) is used.

In these calculations, the initial shape was set to be an ellipsoid, but starting from a perfect sphere does not change the resulting equilibrium shapes. The only difference is in the number of iterations, i.e., the computational cost. In other words, as is typical for nonlinear equation solving in general, the closer the initial point is to solution, the less the computational cost will be. However, for the case where there exist local minima of energy, depending on the minimization algorithms used, initial shape can lead to different equilibrium shapes corresponding to different minima. For example, the spontaneous curvature model has another stable equilibrium oblate shape for reduced volume $v > 0.65$ (see, e.g. [2]) corresponding to a local minimum. So if the initial shape is closer to an oblate shape, the L-BFGS-B minimization used here converges to the oblate instead of the prolate shape. Of course, this is to be expected from any "greedy" descent algorithm like BFGS. Global minimization requires a more robust (and less "greedy") approach such as simulated annealing.

3.1.2. Global constraint enforcement

From the results described above, viscous regularization is shown to significantly lower the computational cost when a penalty method is used to enforce the constraints on area and volume. However, regularization also eliminates the need for *local* enforcement of incompressibility. *Global* constraints on area and volume can be easily implemented via the augmented Lagrangian (AL) method which is generally more efficient than the penalty method. Here, the shape change from the initial ellipsoid shape to the equilibrium shape of $v = 0.9$ is used to compare global enforcement of the constraint on membrane surface area with local enforcement.

Viscous regularization was used with both local and global area constraints. In all cases, the regularization spring constant k was set to be $k = 10\mathcal{K}_C/R_0^2$, where R_0 is the equivalent sphere radius of the vesicle and $\mathcal{K}_C$ is the bending modulus.

Algorithm 2. Hybrid algorithm combining global AL constraint enforcement with viscous regularization

Initialize: p^0, α^0, μ_V^0, μ_A^0, X^0 = initial shape, $\bar{v} = 0.9$ (the specified reduced volume)
Set $n = 0$
repeat
  Minimize $I^n = \Pi[\boldsymbol{x}] + \frac{\mu_V}{2}(V - \overline{V})^2 - p^n V + \frac{\mu_A}{2}(A - \overline{A})^2 + \alpha^n A + I^{\text{reg}}[\boldsymbol{x}; \boldsymbol{X}^n] \rightarrow$ solution, $\boldsymbol{x}^n$
  Update reference: set $\boldsymbol{X}^{n+1} = \boldsymbol{x}^n$
  if $|v_n - \bar{v}|/\bar{v} > \text{TOL}_1$ **then**
    AL Updates:
      $p^{n+1} = p^n - \mu_V^n(V_n - \overline{V})$, $\alpha^{n+1} = \alpha^n + \mu_A^n(A_n - \overline{A})$
      $\mu_V^{n+1} = \mu_V^n \times \text{FAC}$, $\mu_A^{n+1} = \mu_A^n \times \text{FAC}$
  end if
  $n \leftarrow n + 1$
until $|v_n - \bar{v}|/\bar{v} < \text{TOL}_1$ and $I^{\text{reg}}[\boldsymbol{x}^n; \boldsymbol{X}^n] < \text{TOL}_2$

Local enforcement of the area constraint was implemented with a penalty approach as discussed in the previous section. This calculation produced error in reduced volume of $\frac{|v-0.9|}{0.9} \approx 10^{-3}$. Calculations were then

Table 1
Viscous regularization improves the convergence rate of L-BFGS-B minimization. The first row $kR_0^2/\mathcal{K}_C = 0$, shows the results without the viscous regularization, which are identical to the approach used in [17]

$kR_0^2/\mathcal{K}_C$	Total iterations (initial shape $\rightarrow v = 0.9$)	Total iterations ($v = 0.9 \rightarrow 0.8$)
0	35,950	603,858
0.5	2304	287,825
1	1821	9482
10	2122	12,480
100	4776	79,038

k: Spring constant; R_0: equivalent radius of the vesicle; $\mathcal{K}_C$: bending modulus.

performed with Global enforcement of the area constraint, first using a global penalty method, and second using the AL method. In both of the globally constrained calculations, penalty parameters and tolerances were chosen to yield the same accuracy for reduced volume. For the AL implementation, viscous regularization reference updates were included with multiplier updates in a single iteration loop as described in Algorithm 2.

As shown in the Table 2, global constraint enforcement reduced the minimization iteration count by an order of magnitude relative to local enforcement. For this modest level of accuracy the AL implementation was only slightly more efficient than the global penalty implementation. For higher accuracy, $\frac{|v-0.9|}{0.9} \approx 10^{-6}$, wherein the computational cost of local penalty enforcement was prohibitive, global AL enforcement was significantly more efficient than global penalty enforcement.

3.1.3. Non-axisymmetric shapes

Although the shapes of previous example are in fact axisymmetric, the algorithms are fully three-dimensional and can be applied to shapes lacking symmetry. To demonstrate this, the bilayer couple (BC) model [6,7,37] instead of the spontaneous curvature model is used to calculate the equilibrium vesicle shapes over a parameter range in which non-axisymmetric shapes appear as energy minimizers. The BC model modifies the spontaneous curvature model by imposing an additional constraint on the total mean curvature

$$M = \int_{\mathcal{M}} H\sqrt{a}\,\mathrm{d}^2 s, \tag{23}$$

which determines the area difference between the neutral surfaces of the two monolayers of bilayer vesicles. The BC model is defined by the energy (Eq. (7)) together with the three constraints on area, volume and total mean curvature. Hence, the reduced total curvature $m = M/R_0$ (with $R_0 = \sqrt{A/4\pi}$ the equivalent sphere radius) is a third parameter, along with reduced volume and spontaneous curvature,controlling the equilibrium shapes of vesicles, and resulting in some interesting non-axisymmetric configurations (e.g. [2,22]).

For reduced volume $v = 0.8$, four different equilibrium shapes were calculated corresponding to different reduced total curvatures in the range $1.029 \leqslant m/4\pi \leqslant 1.126$, using the same mesh and algorithm as in the previous calculations of the spontaneous curvature model. The resulting shapes, shown in Fig. 3, form a sequence from axisymmetric prolate to non-axisymmetric ellipsoids to axisymmetric oblate, consistent with the traversal across three regions of the equilibrium shape phase diagram in [38].

Table 2
Computational cost of penalty-based local area constraint enforcement vs. the global area constraint enforcement with the penalty and AL methods

Accuracy $\frac{\lvert v-0.9\rvert}{0.9}$	Number of iterations		
	Local penalty	Global penalty	Global AL
10^{-3}	2122	436	425
10^{-6}	–	9231	616

To achieve the same accuracy, global enforcement requires far fewer total iterations than local enforcement. For higher accuracy, the calculation with local penalty enforcement was not completed due to excessive computational cost.

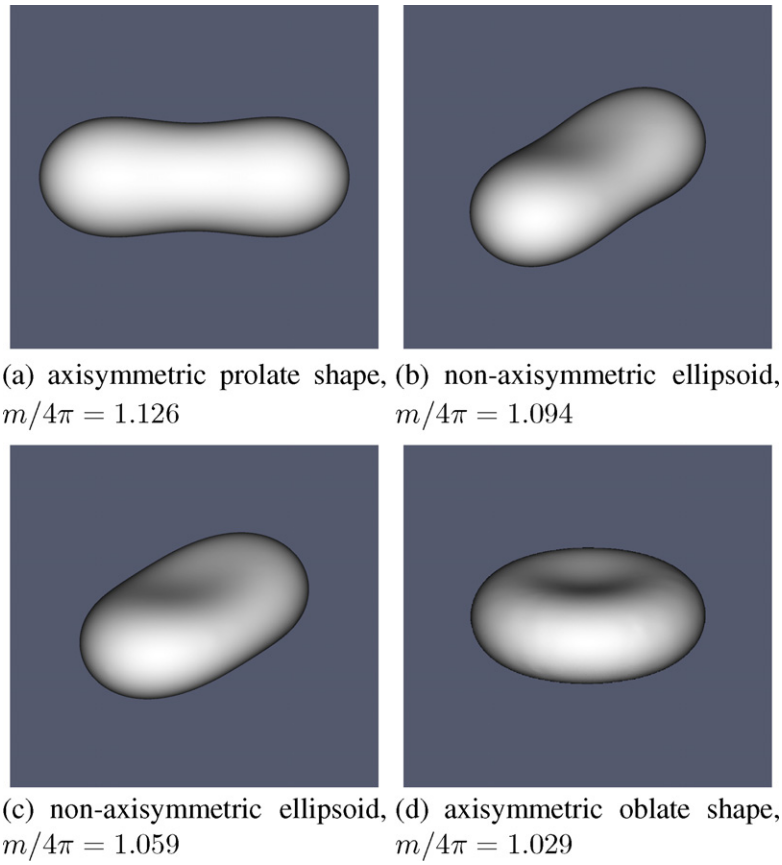

Fig. 3. BC model find different equilibrium shapes for reduced volume $v = 0.8$. Different reduced mean curvature m corresponds to axisymmetric prolate (a), oblate (d) shapes and non-axisymmetric ellipsoids (b) and (c).

3.2. Tether formation

A point force acting on lipid membranes can pull out a long narrow tube commonly called a tether. This can be done by using micropipettes (e.g. [23]), optical tweezers (e.g. [39]), or even growing microtubules inside the vesicle [39]. The mechanical reason for formation of tethers lies in the lack of shearing modulus for membranes. Elongating in one direction and contracting in the other to such a spectacular way like tethers mechanically means extremely large shear deformations [40–43].

Since tether simulation involves very large deformations, the triangles in the finite element mesh are subject to severe distortions. In practice, as elements become more distorted, the zero-energy tangential modes can actually become numerically unstable (Fig. 4). Viscous regularization has to be added in order to suppress these zero-energy modes. Furthermore, the critical force to pull out a tether is very sensitive to pressure and surface tension. Numerically, this necessitates highly accurate enforcement of the volume and area constraints. For a penalty method this implies very large penalty parameters, which lead to conditioning problems. For this reason, here the augmented Lagrangian method is applied.

Starting from an initial equilibrium shape (prolate), tether development is simulated by incrementally displacing nodes at the tips of the vesicle, and performing energy minimization resulting in the equilibrium tethered shapes for each extension. However, even with the viscous regularization, the mesh can still be distorted by the dramatic deformations experienced at larger extensions. Therefore, remeshing is performed at intervals of the extension. Fig. 5 shows snapshots from a typical simulation for reduced volume $v = 0.9$.

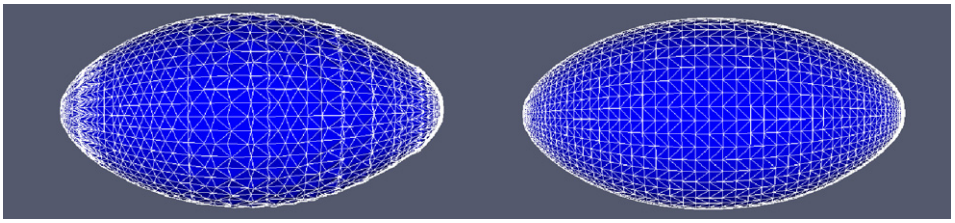

Fig. 4. The equilibrium shape of a vesicle of reduced volume $v = 0.9$ with external forces ($\approx$1 pN) applied at the two ends (forces not shown), mesh without (left figure) and with (right figure) the viscous regularization. Note that the unstabilized mesh is subject to element distortion even at small applied load.

3.2.1. Applied forces

The reaction forces conjugate to specified end displacements can also be calculated by simply adding up all internal forces of the fixed nodes (Eq. (13)). The force vs. end-to-end distance results for the vesicles in Fig. 5 are shown in Table 3, with r the radius of the tethers (μm) and bending modulus $\mathcal{K}_C = 15k_BT$ [39]. Although an exact analytical solution for the force–extension relation is not possible, a simple analytical estimate [41] is used to compare with the computed results from the simulation. The estimate assumes that the thin tube (tether) is pulled out from a sphere, and the sphere remains unchanged during the pulling (Fig. 6). The analytical estimated force and surface tension are given as [41]:

$$F = 2\pi\mathcal{K}_C/r, \tag{24}$$

and the surface tension

$$\alpha = 0.5\mathcal{K}_C/r^2. \tag{25}$$

As Table 3 shows, for well developed tethered shapes (end-to-end distance 11.6 and 12.8 μm, vesicle (e) and (f) in Fig. 5), the computed results and analytical estimations are very close. It is a notable advantage that the present simulation framework is also capable of force–extension calculations for shapes that are not as simple as the schematic in Fig. 6.

3.3. Lipid phase separation

Membranes formed from different lipids can separate into distinct domains (phases) according to their chemical properties, leading to the formation of buds [44,45]. Baumgart et al. [46] found that their experiments are in good agreement with line tension theory [47–49], which treats domain interfaces as sharp with an interface energy proportional to the length of the interface curve. Recently, a phase field computational model was developed for multi-component vesicle membranes combined with the line tension theory [57]. One major drawback of the line tension model is that it requires the system to be pre-phase-separated into well-defined domains, preventing the consideration of composition dynamics. An alternative, smooth-interface approach, based on traditional Ginzburg–Landau (GL) theory [50,51] can be used to also model phase separation [52–56].

Here a GL model for a multi-component bilayer with two different lipids in equilibrium is formulated, assuming that the vesicle is composed of a mixture of two lipids denoted A and B. In general, these two lipid types may have different constitutive properties, as modeled by separate constitutive parameters: $\{\mathcal{K}_C^{(A)}, \mathcal{K}_G^{(A)}, C_0^{(A)}\}$ for lipid A, and $\{\mathcal{K}_C^{(B)}, \mathcal{K}_G^{(B)}, C_0^{(B)}\}$ for lipid B. Let the local concentrations of the two lipids be described by the concentration parameters $c^{(A)}$, $c^{(B)} \in [0,1]$ with $c^{(A)} + c^{(B)} = 1$. The local lipid concentration at point $\mathsf{s} = (s^1, s^2)$ can then be described by an order-parameter field $c(\mathsf{s}) \equiv c^{(A)}$, which is referred to as the concentration field or phase field. The local constitutive properties of the membrane can then be modeled as functions of the phase field with convex combinations of the pure phase parameters:

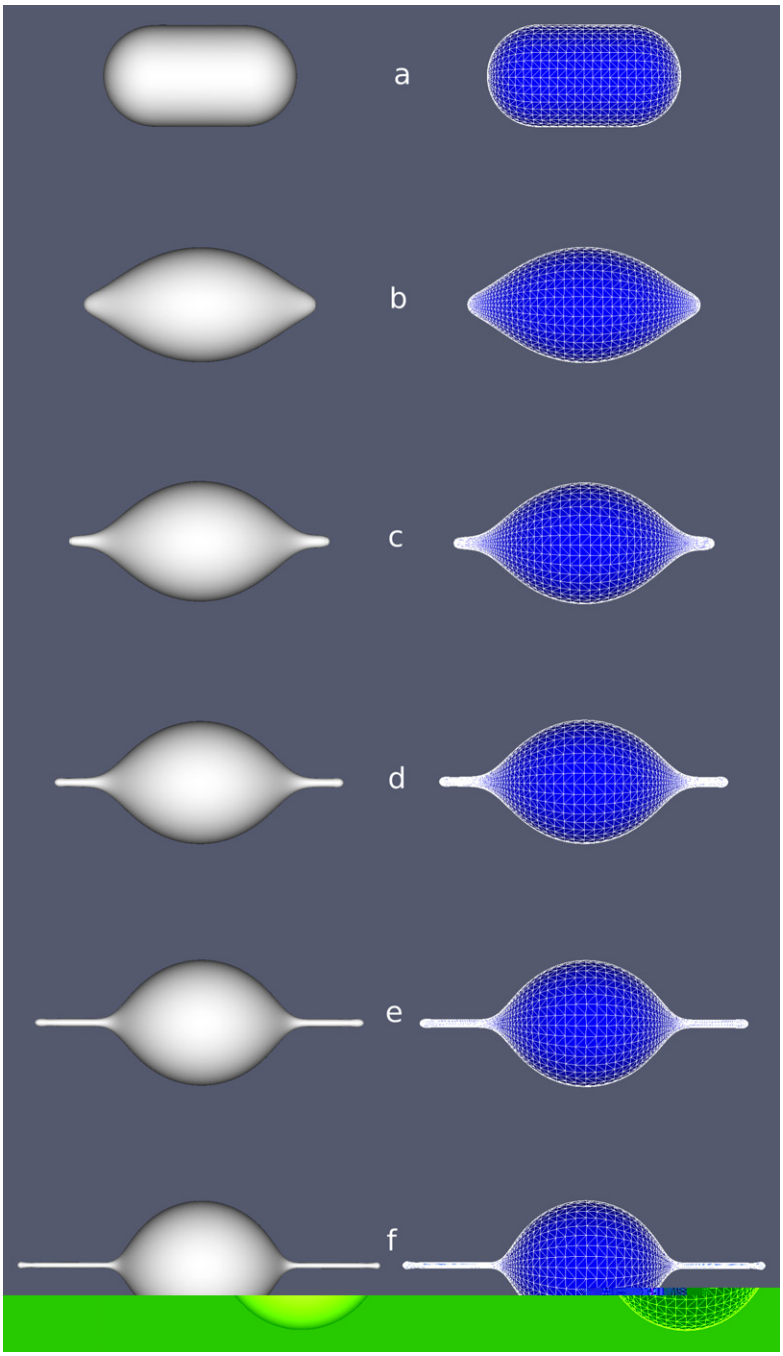

Fig. 5. The tethering of a vesicle starting from a prolate of reduced volume $v = 0.9$. (left) Limit surfaces of equilibrium shapes; (right) control meshes. Number of nodes and elements: (a) 4202 nodes, 8400 elements; (b) and (c) 4682 nodes, 9360 elements; (d) 6202 nodes, 12,400 elements; (e) and (f) 8682 nodes, 17,360 elements. End-to-end distance: (a) 6.8 μm, (b) 8.2 μm, (c) 9.2 μm, (d) 10.2 μm, (e) 11.6 μm and (f) 12.8 μm.

Table 3
Computed and analytical estimated forces for each tethered shape

End-to-end distance (μm)	6.8	8.2	9.2	10.2	11.6	12.8
Computed tether radius (μm)	n/a	n/a	0.20	0.165	0.140	0.105
Computed force (pN)	0	1.41	1.76	2.14	2.72	3.68
Analytical estimated force (pN)	n/a	n/a	1.88	2.29	2.69	3.59
Computed tension (pN/μm)	0.05	0.43	0.71	0.98	1.60	2.93
Analytical estimated tension (pN/μm)	n/a	n/a	0.75	1.10	1.53	2.72

For the shape in Fig. 5c, the computed tether radius is not uniform along the extension direction, and $r = 0.20$ μm is an estimate. As noted in the text a bending modulus of $\mathcal{K}_C = 15k_BT$ is used for all calculations.

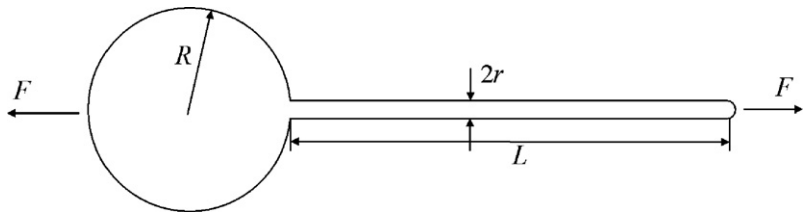

Fig. 6. Schematic of the tethered shape.

$$\mathcal{K}_C = c\mathcal{K}_C^{(A)} + (1-c)\mathcal{K}_C^{(B)}, \tag{26a}$$

$$\mathcal{K}_G = c\mathcal{K}_G^{(A)} + (1-c)\mathcal{K}_G^{(B)}, \tag{26b}$$

$$C_0 = cC_0^{(A)} + (1-c)C_0^{(B)}. \tag{26c}$$

Thus, rewriting the strain energy including explicit dependence of fields on surface position,

$$E = \int_{\mathcal{M}} \left\{ \frac{1}{2}\mathcal{K}_C(\mathsf{s})[2H(\mathsf{s}) - C_0(\mathsf{s})]^2 + \mathcal{K}_G(\mathsf{s})K(\mathsf{s}) \right\} \sqrt{a}\, \mathrm{d}^2 s \tag{27}$$

where explicit dependence of the mechanical properties on surface coordinates s has been noted as a reminder of the heterogeneity of the system.

One further modification to the energy functional is needed to build into the model of the physics of phase separation [51]:

$$I = E + \int_{\mathcal{M}} [\Delta E \psi(c) + \epsilon |\nabla c|^2] \sqrt{a}\, \mathrm{d}^2 s. \tag{28}$$

Here the normalized GL energy $\psi(c)$ is a double-well potential such as

$$\psi(c) = 16c^2(c-1)^2$$

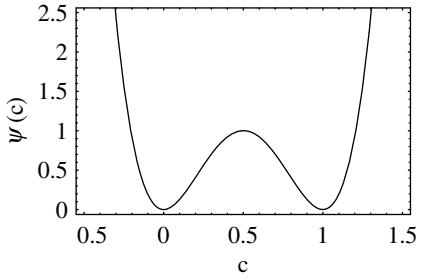

Fig. 7. Double-well normalized GL energy $\psi(c) = 16c^2(c-1)^2$ used to model phase segregation in a two-component lipid system.

(see Fig. 7) which is minimized when the concentration c takes a value of either 0 or 1, corresponding to local lipid concentration of either pure type A or pure type B. The parameter ΔE scales the height of the barrier between the two minima of $\psi(c)$, and controls the energy cost of a domain interface. The second addition to the energy describes short-range cooperativity between neighboring lipids. The parameter ϵ is essentially a length scale which will determine the width of the region of transition between phases. As ϵ decreases to zero, this region will limit to a curve where the concentration gradient can be non-zero. Inclusion of this penalty term in the energy will then produce the effect of a diffuse line tension in the transition between regions of pure phases.

The mechanics of the membrane are then dependent on both the shape of the vesicle and the lipid composition. Minimization of the total potential energy now yields two sets of Euler–Lagrange equations, one being

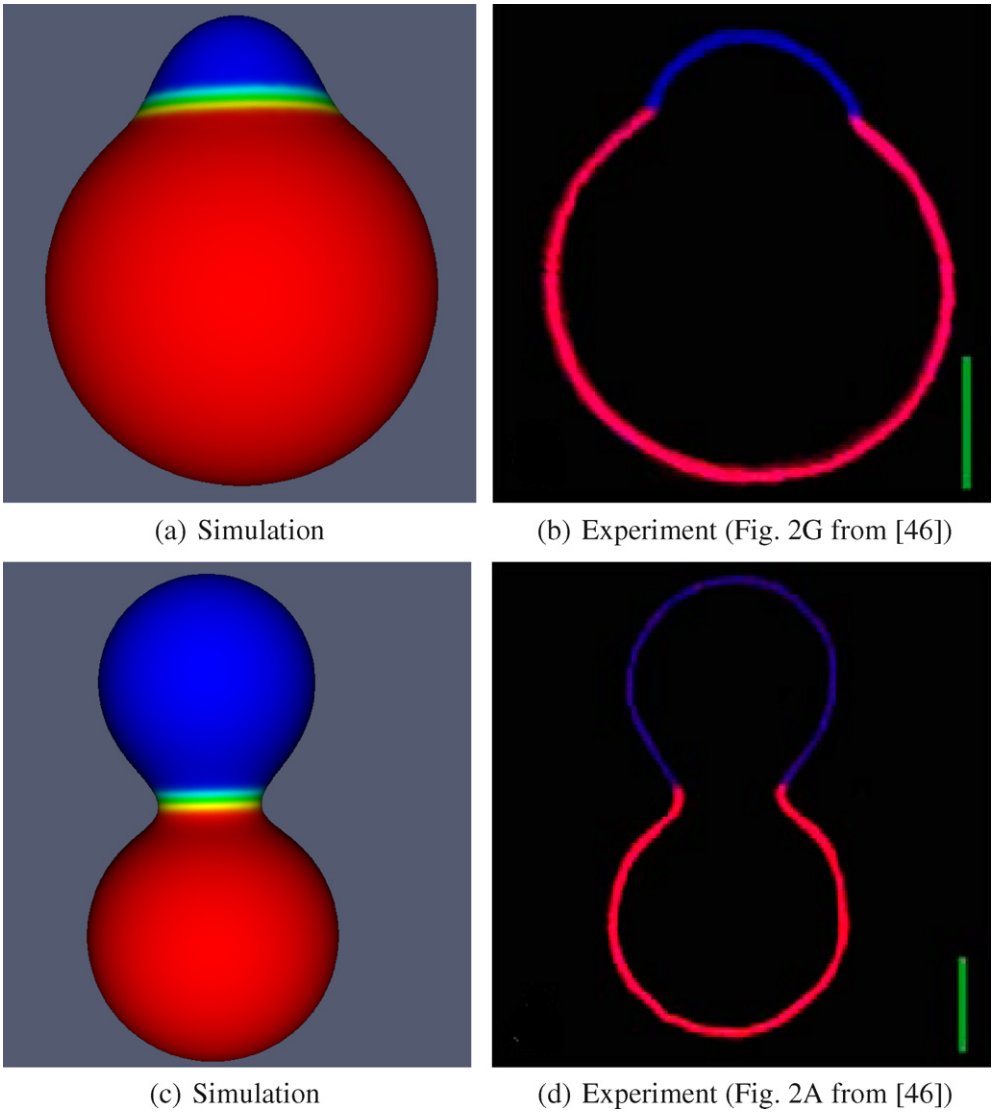

Fig. 8. Comparison of simulation and experiment for two component lipid phase separation. (a) and (b) have reduced volume $v = 0.98$ and global concentration $x_B = 0.89$. (c) and (d) have $v = 0.76$ and $x_B = 0.56$. Phase A ($c = 0$) is colored blue; phase B ($c = 1$) is colored red. Scale bars are 5 μm. Experimental images are taken from the work of Baumgart et al. [46]. (For interpretation of the references in color in this figure legend, the reader is referred to the web version of this article.)

the equilibrium equations related to variations in the shape $\delta \boldsymbol{x}$, and the other being a phase equilibrium equation related to variations in the concentration δc.

Using this GL framework for two-component vesicles, we simulated mechanical and phase equilibrium for two vesicles from Fig. 2A and G in [46]. The first of these had reduced volume $v = 0.98$ and phase B area fraction $x_B = (1/A)\int c\,\mathrm{d}A = 0.89$; the second had $v = 0.76$ and $x_B = (1/A)\int c\,\mathrm{d}A = 0.56$. Each simulation started from an originally spherical mesh with two separate domains. For consistency with the experimental work of Baumgart et al. [44,46], the bending moduli were set to $\mathcal{K}_C^{(B)} \approx 10^{-19}$ J, $\mathcal{K}_C^{(A)} = 5\mathcal{K}_C^{(B)}$, $\mathcal{K}_G \approx -\mathcal{K}_C$; the line tension taken as $\sigma \approx 10^{-12}$ N; and the equivalent radius of the vesicles set to $R_0 = \sqrt{A/4\pi} \approx 10\ \mu\mathrm{m}$.

The GL theory [50,51] relates the two parameters ΔE and ϵ to the line tension σ and the width of the transition region between the two phases δ via the scalings $\sigma \sim \sqrt{\Delta E \epsilon}$, and $\delta \sim \epsilon/\Delta E$. Setting $\delta = R_0/10$, the given value of line tension sets the values of the two GL parameters as $\Delta E = 1000\mathcal{K}_C^{(B)}/R^2,\ \epsilon = 10\mathcal{K}_C^{(B)}$.

As shown in Fig. 8, the simulated shapes and phase distributions agree qualitatively well with those of the experiments. For the $v = 0.98$ vesicle, the simulation captured the small cap seen in the experiment (Fig. 8a and b). Similarly, the $v = 0.76$ vesicle experiences a "necking" deformation at the phase interface in the equatorial region. As a result, the deformed mesh around the interface was heavily distorted when simulated using the dashpot-style viscous regularization technique (Fig. 9a). Because the simulation starts from a sphere with roughly equilateral triangle elements, the shape change of vesicle causes the elements in the interface region to contract severely in the circumferential direction. This element distortion needs to be suppressed because it can lead to inaccuracy and instability of the finite element simulation.

In order to retain a high-quality mesh after the deformation, the elements near the interface need to contract in all directions so that they remain roughly equilateral, resulting in a greater *density* of elements than in other parts of the vesicle. To tackle such large deformations, remeshing strategies are often needed. The viscous regularization introduced in Section 2.2 makes an r-adaptive remeshing possible, since reference config-

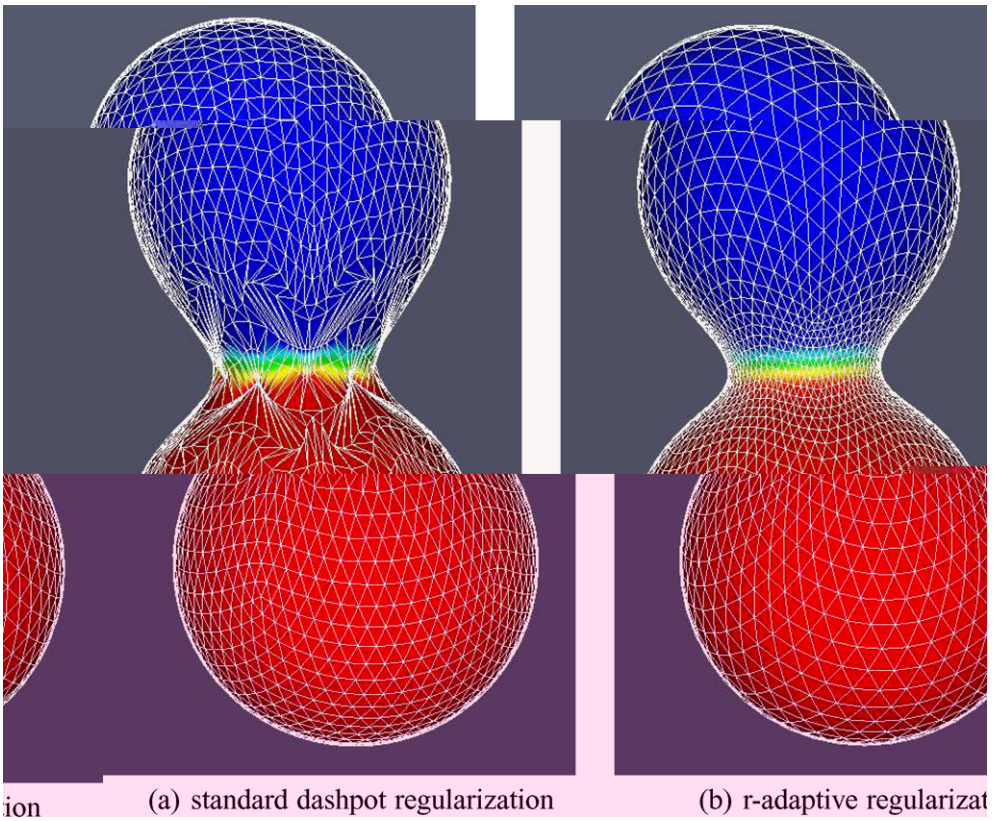

Fig. 9. r-Adaptive regularization helps elements perform well in the interface ($v = 0.76$).

uration can be arbitrarily formulated to reposition the nodes of the mesh. Here, a slight modification of the dashpot regularization method is proposed with a reference updating strategy that drives elements toward equilateral shape.

Given an element of the mesh at regularization iteration $n-1$ with area A^{n-1}, r-adaptive regularization at step n is defined by placing springs on the three edges all of the same reference length

$$\bar{\ell}^{n-1} = 2\sqrt{\frac{A^{n-1}}{\sqrt{3}}},$$

i.e., the length of a side of an equilateral triangle of the same area A_{n-1}. Thus the regularization energy term for each triangle is written as

$$E_n = \frac{k}{2}\sum_{i=1}^{3}(\ell_i^n - \bar{\ell}^{n-1})^2, \tag{29}$$

where the ℓ_i are the lengths of the element edges.

In principle this regularization energy could be applied to every element in a mesh. However, in practice these iterative updates are slow to converge to a fully relaxed state (with zero regularization energy), and depending on the regularization constant k and initial mesh quality the method can get stuck in a state with finite energy stored in the springs. Indeed there is no clear interpretation of this modified form as a time-discretization of any viscous PDE, and therefore no theoretical guarantee of convergence of regularizing forces to zero. Hence, to obtain such convergence in practice, this "equilateral" form of the dashpot regularization should only be applied selectively to poorly shaped elements, and in such a way that once all elements attain sufficient shape quality the standard viscous regularization can take over globally.

In our implementation, a shape criteria γ is formulated to calculate different spring energy for different elements,

$$\gamma = (1/\bar{\ell}^2)\sum_{i=1}^{3}(\ell_i - \bar{\ell})^2.$$

Using this measure of shape quality, the regularization energy is defined for each triangle by

$$E_n = \begin{cases} \frac{k}{2}\sum_{i=1}^{3}(\ell_i^n - \bar{\ell}^{n-1})^2, & \gamma \text{ large}, \\ \frac{k}{2}\sum_{i=1}^{3}(\ell_i^n - \ell_i^{n-1})^2, & \gamma \text{ small}. \end{cases} \tag{30}$$

In other words, if γ is large (say, $\gamma > 1$) for an element, it has poor shape and r-adaptive regularization is used on that element; if γ is small enough, reference lengths are updated from the deformed lengths of the previous iteration as for the dashpot model described earlier. In practice, after several reference updates, all the elements attain a sufficiently small γ and the regularization algorithm switches everywhere to the dashpot model. The addition of r-adaptive regularization has the effect of initially "driving" the nodes around on the membrane surface so as to achieve higher-quality element shapes.

In the present example of a phase-separated vesicle at $v = 0.76$, this results in a finer mesh of smaller element sizes near the interface area (Fig. 9b), consistent with the shrinking of the interface due to "line tension" effects. Although the "equilateral" form of regularization triggered in this simulation by distortion of elements near the interface initially produced unphysical tangential "driving forces" on the nodes, iterative reference updating allowed an eventual switch to the purely viscous dashpot-type regularization and ultimate convergence of tangential forces to zero. The simulated result is compared with the experimental data of Fig. 8 in [46].

As a final note, when applying the r-adaptive scheme some attention should be paid in choosing a target element quality – i.e., the tolerance for γ in Eq. (30). In our experience, applying r-adaptive regularization for $\gamma > 0.2$ in all cases produced good quality meshes with regularization forces converging to zero after a reasonable number of reference updates. More aggressive tolerances for γ could perhaps lead to "locked in" regularization forces not converging to zero after a large number of reference updates. However, we have yet to see such behavior from the method of Eq. (30).

4. Conclusions

[13] L. Hsu, R. Kusner, J. Sullivan, Minimizing the squared mean curvature integral for surfaces in space forms, Exp. Math. 1 (3) (1992) 191–207.
[14] M. Jaric, U. Seifert, W. Wintz, M. Wortis, Vesicular instabilities: the prolate-to-oblate transition and other shape instabilities of fluid bilayer membranes, Phys. Rev. Lett. 52 (1995) 6623.
[15] M. Kraus, U. Seifert, R. Lipowsky, Gravity-induced shape transformations of vesicles, Europhys. Lett. 32 (5) (1995) 431–436.
[16] W. Wintz, H.-H. Döbereiner, U. Seifert, Starfish vesicles, Europhys. Lett. 33 (1996) 403–408.
[17] F. Feng, W.S. Klug, Finite element modeling of lipid bilayer membranes, J. Comput. Phys. 220 (2006) 394–408.
[18] G. Gompper, D.M. Kroll, Network models of fluid, hexatic and polymerized membranes, J. Phys.: Condens. Matter 9 (1997) 8795–8834.
[19] R. Capovilla, J. Guven, J.A. Santiago, Deformations of the geometry of lipid vesicles, J. Phys. A: Math. Gen. 36 (2003) 6281–6295.
[20] J.-S. Ho, A. Baumgärtner, Simulations of fluid self-avoiding membranes, Europhys. Lett. 12 (4) (1990) 295–300.
[21] H. Noguchi, G. Gompper, Dynamics of fluid vesicles in shear flow: effect of membrane viscosity and thermal fluctuations, Phys. Rev. E 72 (2005) 0119011–0119014.
[22] V. Heinrich, S. Saša, B. Žekš, Nonaxisymmetric vesicle shapes in a generalized bilayer-couple model and the transition between oblate and prolate axisymmetric shapes, Phys. Rev. E 48 (4) (1993) 3112–3123.
[23] V. Heinrich, B. Božič, S. Saša, B. Žekš, Vesicle deformation by an axial load: from elongated shapes to tethered vesicles, Biophys. J. 76 (1999) 2056–2071.
[24] Q. Du, C. Liu, X. Wang, A phase field approach in the numerical study of the elastic bending energy for vesicle membranes, J. Comput. Phys. 198 (2004) 450–468.
[25] Q. Du, C. Liu, X. Wang, Simulating the deformation of vesicle membranes under elastic bending energy in three dimensions, J. Comput. Phys. 212 (2) (2006) 757–777.
[26] H. Noguchi, G. Gompper, Meshless membrane model based on the moving least-squares method, Phys. Rev. E 73 (2006) 021903.
[27] I.S. Sokolnikoff, Tensor Analysis: Theory and Applications to Geometry and Mechanics of Continua, second ed., Wiley, New York, 1964.
[28] M. Do Carmo, Differential Geometry of Curves and Surfaces, Prentice Hall, 1976.
[29] J. Nocedal, S.J. Wright, Numerical Optimization, Springer-Verlag, 1999.
[30] F. Cirak, M. Ortiz, P. Schröder, Subdivision surfaces: a new paradigm for thin-shell finite-element analysis, Int. J. Numer. Method Eng. 47 (2000) 2039–2072.
[31] F. Cirak, M. Ortiz, Fully c^1-conforming subdivision elements for finite deformation thin-shell analysis, Int. J. Numer. Method Eng. 51 (2001) 813–833.
[32] D.J. Steigmann, Fluid films with curvature elasticity, Arch. Rational Mech. Anal. 150 (1999) 127–152.
[33] E.A. Evans, R. Skalak, Mechanics and Thermodynamics of Biomembranes, CRC Press, Boca Raton, FL, 1980.
[34] R.H. Byrd, P. Lu, J. Nocedal, C. Zhu, A limited memory algorithm for bound constrained optimization, SIAM J. Sci. Comput. 16 (5) (1995) 1190–1208.
[35] C. Zhu, R.H. Byrd, P. Lu, J. Nocedal, Algorithm 778: L-bfgs-b: Fortran subroutines for large-scale bound-constrained optimization, ACM Trans. Math. Softw. 23 (4) (1997).
[36] Free L-BFGS-B software. Available at <http://www.ece.northwestern.edu/~nocedal/lbfgsb.html>.
[37] S. Svetina, B. Zeks, Membrane bending energy and shape determination of phospholipid vesicles and red blood cells, Eur. Biophys. J. 17 (2) (1989) 101–111.
[38] U. Seifert, K. Berndl, R. Lipowsky, Shape transformations of vesicle-phase-diagram for spontaneous-curvature and bilayer-coupling models, Phys. Rev. A 44 (1991) 1182–1202.
[39] D.K. Fygenson, J.F. Marko, A. Libchaber, Mechanics of microtubule-based membrane extension, Phys. Rev. Lett. 79 (1997) 4497–4500.
[40] B. Božič, S. Svetina, B. Žekš, Theoretical analysis of the formation of membrane microtubes on axially strained vesicles, Phys. Rev. E 55 (5) (1997) 5834–5842.
[41] I. Derényi, F. Jülicher, J. Prost, Formation and interaction of membrane tubes, Phys. Rev. Lett. 88 (23) (2002) 238101–238104.
[42] T.R. Powers, G. Huber, R.E. Goldstein, Fluid-membrane tethers: minimal surfaces and elastic boundary layers, Phys. Rev. E 65 (4) (2002) 041901–041911.
[43] A.S. Smith, E. Sackmann, U. Seifert, Pulling tethers from adhered vesicles, Phys. Rev. Lett. 92 (20) (2004) 208101–208104.
[44] T. Baumgart, S.T. Hess, W.W. Webb, Imaging coexisting fluid domains in biomembrane models coupling curvature and line tension, Nature 425 (2003) 821–824.
[45] K. Bacia, P. Schwille, T. Kurzchalia, Sterol structure determines the separation of phases and the curvature of the liquid-ordered phase in model membranes, Proc. Natl. Acad. Sci. USA 102 (2005) 3272–3277.
[46] T. Baumgart, S. Das, W.W. Webb, T. Jenkins, Membrane elasticity in giant vesicles with fluid phase coexistence, Biophys. J. 89 (2005) 1067–1080.
[47] R. Lipowsky, Budding of membranes induced by intramembrane domains, J. Phys. II (France) 2 (1992) 1825–1840.
[48] F. Jülicher, R. Lipowsky, Domain-induced budding of vesicles, Phys. Rev. Lett. 70 (19) (1993) 2964–2967.
[49] F. Jülicher, R. Lipowsky, Shape transitions of vesicles with intramembrane domains, Phys. Rev. E 53 (1996) 2670–2683.
[50] R.W. Balluffi, S.M. Allen, W.C. Carter, Kinetics of Materials, John Wiley & Sons Inc., Hoboken, NJ, 2005.
[51] J.C. Toledano, P. Toledano, The Landau Theory of Phase Transitions, World Scientific, Singapore, 1987.
[52] T. Kawakatsu, D. Andelman, K. Kawasaki, T. Taniguchi, Phase transitions and shapes of two component membranes and vesicles. I: Strong segregation limit, J. Phys. II (France) 3 (1993) 971–997.

[53] T. Taniguchi, K. Kawasaki, D. Andelman, T. Kawakatsu, Phase transitions and shapes of two component membranes and vesicles. II: Weak segregation limit, J. Phys. II (France) 4 (1994) 1333–1362.
[54] T. Taniguchi, Shape deformation and phase separation dynamics of two-component vesicles, Phys. Rev. Lett. 76 (23) (1996) 4444–4447.
[55] G.S. Ayton, J.L. McWhirter, P. McMurtry, G.A. Voth, Coupling field theory with continuum mechanics: a simulation of domain formation in giant unilamellar vesicles, Biophys. J. 88 (6) (2005) 3855–3869.
[56] Y. Jiang, T. Lookman, A. Saxena, Phase separation and shape deformation of two-phase membranes, Phys. Rev. E 61 (1) (2000) 57–60.
[57] X. Wang, Q. Du, Modeling and simulations of multi-component lipid membranes and open membranes via diffuse interface approaches, J. Math. Biol. 56 (2008) 347–371.
[58] T.G. Frey, C.A. Mannella, The internal structure of mitochondria, Trends Biochem. Sci. 25 (2000) 319–324.
[59] E.L. Snapp, R.S. Hegde, M. Francolini, F. Lombardo, S. Colombo, E. Pedrazzini, N. Borgese, J. Lippincott-Schwartz, Formation of stacked ER cisternae by low affinity protein interactions, J. Cell Biol. 163 (2) (2003) 257–269.